Nanoscale Advances

ROYAL SOCIETY OF CHEMISTRY

PAPER

View Article Online
View Journal | View Issue

Check for updates

Cite this: *Nanoscale Adv.*, 2026, **8**, 1260

A durable MoS_2-BN/cellulose acetate photocatalyst for sustainable removal of organic pollutants *via* heterogeneous multilayer adsorption

S. M. Neeraja,[a] B. Bindhu,*[a] Jebiti Haribabu,[b] R. Ramesh, *[c] Abdullah Al Souwaileh,[d] Perumal Naveenkumar,[e] Arunachalam Arulraj,[f] Daniel Moraga[g] and Adhigan Murali[h]

In this study, we introduce a novel technique for creating a Molybdenum Disulphide f-Boron Nitride (MoS_2-(f-BN)) impregnated Cellulose Acetate (CA) composite with enhanced photodegradation properties for use in water treatment. The material comprises a heterostructure of functionalized boron nitride (f-BN) and molybdenum disulphide (MoS_2), synthesized within a cellulose acetate (CA) matrix. XRD, FT-IR, UV-vis, BET, TG-DTA, Raman, and PL investigations are among the extensive structural and optical characterization methods that verify the successful synthesis of the composite with a lowered bandgap of 3.3 eV, hence increasing its photocatalytic activity. Using a new MoS_2@(f-BN)@CA composite, this work examines the photocatalytic degradation of Crystal Violet (CV) dye when exposed to sunshine. The composite showed notable photocatalytic activity. Variables like irradiation time, pH, dye concentration, and catalyst dose were used to assess CV's degrading efficiency. The degradation reached over 86% after 120 minutes, according to the results, which increased with irradiation time. The composite performed best close to a pH of 6, which is neutral. The composite remained significantly active at all tested concentrations, despite the fact that greater dye concentrations initially caused more deterioration. CV elimination was also improved by raising the catalyst dosage. Adsorption investigations showed that the composite's adsorption behavior adhered to the Freundlich isotherm model, suggesting multilayer adsorption and a heterogeneous adsorption surface. The composite's heterogeneous composition and favorable adsorption were validated using the Freundlich isotherm characteristics. These results demonstrate the MoS_2@(f-BN)@CA composite's potential as an efficient and long-lasting photocatalyst for water purification applications, underscoring its viability for environmental remediation.

Received 27th August 2025
Accepted 17th December 2025

DOI: 10.1039/d5na00830a

rsc.li/nanoscale-advances

Open Access Article. Published on 19 December 2025. Downloaded on 4/5/2026 8:17:09 PM.
This article is licensed under a Creative Commons Attribution-NonCommercial 3.0 Unported Licence.

1 Introduction

The escalating global discharge of highly persistent and toxic organic dye pollutants into aquatic ecosystems represents a profound environmental and public health crisis. Traditional physical and chemical remediation methods, such as adsorption and coagulation, often involve high operational energy costs and complex procedures, and ultimately lead to the generation of large volumes of secondary toxic sludge.[1] The necessity for sustainable and efficient alternatives has brought the field of photocatalytic degradation to the forefront of research.[2] As a powerful Advanced Oxidation Process (AOP), photocatalysis utilizes semiconductor materials to harvest light energy and generate highly reactive oxygen species (ROS)[3] capable of mineralizing complex organic contaminants completely into harmless end products, primarily H_2O and CO_2. The reliance on solar illumination positions photocatalysis as an economically compelling and environmentally benign solution for large-scale water remediation.[4]

[a]*Department of Physics, Noorul Islam Centre for Higher Education, Kumaracoil, Thuckalay, 629180, Tamil Nadu, India. E-mail: bindhu.krishna80@gmail.com*
[b]*Facultad de Medicina, Universidad de Atacama, Los Carreras 1579, 1532502 Copiapo, Chile*
[c]*Department of Chemical Engineering, School of Mechanical, Chemical and Material Engineering, Adama Science and Technology University, Adama, P.O. Box-1888, Adama, Ethiopia. E-mail: ramesh.redrouthu@astu.edu.et*
[d]*Department of Chemistry, College of Science, King Saud University, Riyadh 11451, Saudi Arabia*
[e]*Metal-organic Compounds Materials Research Center, Sejong University, 209, Neungdong-ro, Gwangjin-gu, Seoul 05006, The Republic of Korea*
[f]*Departamento de Electricidad, Facultad de Ingeniería, Universidad Tecnológica Metropolitana (UTEM), Av. José Pedro Alessandri 1242, Ñuñoa 7800002, Santiago, Chile*
[g]*Laboratorio de Fisiología, Departamento de Ciencias Biomédicas, Facultad de Medicina, Universidad de Tarapacá, Arica 1000000, Chile*
[h]*Center for Global Health Research, Saveetha Medical College and Hospital, Saveetha Institute of Medical and Technical Sciences, Saveetha University, Chennai, Tamil Nadu, India*

© 2026 The Author(s). Published by the Royal Society of Chemistry

Open Access Article. Published on 19 December 2025. Downloaded on 4/5/2026 8:17:09 PM.
This article is licensed under a Creative Commons Attribution-NonCommercial 3.0 Unported Licence.

Despite the fundamental promise of photocatalytic materials, their widespread commercialization is significantly hindered by two major, interconnected materials science deficiencies, which define the critical research gap. First, the intrinsic efficiency of many single-component semiconductors is severely limited by the ultra-fast recombination rate of photogenerated electron–hole pairs.[5] This short lifespan of charge carriers dramatically lowers the quantum yield and the steady-state concentration of the powerful ROS required for effective contaminant mineralization. Second, while the advancement of nanostructured materials offers excellent surface area and activity, they present severe practical impediments. These fine powders often exhibit poor chemical stability, low dispersibility in water, and are exceptionally difficult to separate, recover, and reuse after treatment using conventional filtration techniques. This lack of facile recyclability makes them unsuitable for continuous, long-term industrial processes. Successfully addressing these constraints requires the rational design of sophisticated multi-functional hybrid nanocomposites that can simultaneously enhance charge separation kinetics and provide a practical mechanism for easy recovery and structural stabilization.

Recent research has heavily focused on utilizing two-dimensional (2D) nanomaterials, like Molybdenum Disulphide (MoS_2) and Boron Nitride (BN), to construct high-performance hybrid photocatalysts.[6] MoS_2, a transition metal dichalcogenide, is highly regarded for its tunable narrow bandgap (1.2–1.9 eV), which provides superior visible light absorption compared to traditional wide-bandgap semiconductors (*e.g.*, TiO_2).[7] Furthermore, its layered structure exposes numerous active edge sites crucial for heterogeneous catalysis. However, MoS_2 nanosheets on their own are susceptible to aggregation and photo-corrosion. In contrast, Boron Nitride (BN), structurally analogous to graphene, possesses exceptional chemical and thermal stability, acting as an excellent electronic insulator and support material. The integration of MoS_2 and BN into a heterostructure is a powerful strategy to overcome the charge recombination issue, as the Fermi level difference between the two components facilitates the rapid, directional migration of photogenerated electrons and holes, maximizing their lifespan and boosting ROS generation.[8] While this MoS_2/BN combination addresses the mechanistic challenge, the practical issue of recovery in aqueous systems remains. This necessitates the use of a robust, non-toxic, and macroscopic support. Cellulose Acetate (CA), a globally abundant, biodegradable, and high-strength biopolymer, is an ideal candidate matrix for composite fabrication, as it provides the crucial mechanical support and the means for easy handling and recovery, thereby satisfying the sustainability requirement for industrial applications.[9]

To realize a truly practical and efficient photocatalytic system, this work introduces a novel, three-component hybrid: the MoS_2@(f-BN)@CA nanocomposite. Engineered *via* a strategic solution casting technique, this composite is designed to deliver synergistic enhancement across all necessary criteria. Molybdenum disulphide (MoS_2) serves as the core visible light absorber and catalyst. Specifically, a unique surface functionalization strategy was employed on the boron nitride nanosheets using cetyl alcohol, yielding f-BN that maximized chemical compatibility and π–π interactions with MoS_2, ensuring the formation of a robust heterojunction.[10] This functionalization is key to forming a stable and highly efficient MoS_2/(f-BN) heterostructure, which accelerates charge separation, effectively inhibiting recombination and maximizing ROS production. Finally, the entire active MoS_2@(f-BN) system is robustly embedded within the flexible, non-toxic Cellulose Acetate (CA) matrix. The CA matrix provides indispensable mechanical strength and allows the composite to be easily fabricated into a recoverable film or membrane-like structure, ensuring facile separation and excellent reusability for multiple catalytic cycles.[11] This manuscript details the synthesis, and structural and optoelectronic characterization of the MoS_2@(f-BN)@CA nanocomposite. We then rigorously evaluate its superior photocatalytic performance for the degradation of Crystal Violet (CV) dye, a model cationic dye, under visible light irradiation. The demonstrated results validate the synergistic material design, confirming that this novel, stable, and recoverable hybrid offers a highly promising and scalable solution for advanced photocatalytic wastewater remediation.

2 Experimental section

2.1 Materials

All chemicals used in this study were purchased from Sigma-Aldrich, USA (AR Grade): boron nitride (molecular weight: 24.82 g mol^{-1}, 99% purity AR grade), molybdenum disulphide (molecular weight: 160.06 g mol^{-1}), cetyl alcohol (molecular weight: 242.41 g mol^{-1}), cellulose acetate, acetone (58.08 g mol^{-1}), DMF (dimethyl formamide) (molecular weight: 73.10 g mol^{-1}, 99% purity), deionized water.

2.2 Preparation of MoS_2/f-BN and MoS_2@(f-BN)@CA

Liquid phase exfoliation was used to separate the nanosheets from their bulk counterparts in BN and MoS_2. For the fabrication of the MoS_2@f-BN hybrid, BNNS nanosheets were functionalized with cetyl alcohol to enhance their dispersion and interfacial compatibility. The pre-functionalized BN was then re-distributed in water and sonicated to guarantee uniform dispersion. Separately, MoS_2 nanosheets were exfoliated and dissolved in water under similar conditions. To guarantee correct mixing, the two dispersions were then combined and vigorously agitated. Strong contacts between the MoS_2 and f-BN were promoted by prolonged stirring, which aided in the hybridization process. MoS_2@f-BN, the resultant hybrid composite, was separated by centrifugation or filtration and then dried to produce a powder. To create a homogeneous solution, enough cellulose acetate (CA) was dissolved in acetone. In order to obtain a uniform dispersion, a suitable amount of MoS_2@f-BN was forcefully swirled. After that, the suspension was centrifuged to get rid of any aggregates and encourage better component integration. The final MoS_2@(f-BN)@CA composite was obtained by carefully drying the synthesized composite in a hot oven to eliminate any leftover

Open Access Article. Published on 19 December 2025. Downloaded on 4/5/2026 8:17:09 PM.
This article is licensed under a Creative Commons Attribution-NonCommercial 3.0 Unported Licence.

solvent. After that, this substance was used in water treatment applications.

2.3 Measurements

The morphological characteristics of the samples were examined using a Field Emission Scanning Electron Microscope (FE-SEM, JSM7600F, Jeol). XRD patterns were analyzed using an X-PERT-PRO X-ray diffractometer equipped with a CuKα source (λ = 1.5218 Å). A Thermo Scientific Nicolet IS50 Quest ATR-specac Bruker-Alpha ATR was used for FTIR measurements in an effort to determine structural compositions. UV-visible adsorption studies were conducted using a UV-visible spectrometer from PerkinElmer. A HORIBA JOBIN YVON T6400 was the instrument used to obtain the Raman spectrum of the samples. Photodegradation studies were carried out using a UV-vis spectrometer. BET analysis was carried out using Quantachrome® ASiQwin™ automated gas sorption data acquisition and reduction software from Quantachrome Instruments.

2.4 Investigations on photocatalytic activity and active species

While altering important photocatalytic parameters, the photocatalytic efficiency of MoS_2@(f-BN)@CA was assessed for the degradation of Crystal Violet dye in the presence of sunlight. 0.2 g of MoS_2@(f-BN)@CA was dispersed in 100 mL of an aqueous crystal violet solution with an initial concentration of 5 mg L^{-1} as part of the experimental process. To achieve adsorption–desorption equilibrium, the reaction mixture was constantly agitated without light using a magnetic stirrer. The suspension was exposed to direct sunshine to start the photocatalytic breakdown process after equilibrium was reached. To separate the photocatalytic particles, 5 mL aliquots of the reaction mixture were taken out and centrifuged at predetermined intervals. A UV-vis spectrometer (Shimadzu UV-1800) was then used to measure the absorbance at the distinctive wavelength of 664 nm in order to analyze the supernatant. The degradation efficiency of the dye was determined using the formula

$$\%\ \text{Degradation} = \left(\frac{A_0 - A}{A_0}\right)100 \quad (1)$$

A_0 = initial absorbance of dye, A = absorbance of dye solution after solar irradiation.

3 Results and discussion

The XRD patterns of MoS_2@f-BN and MoS_2@(f-BN)@CA are shown in Fig. 1. Fig. 1a shows distinct peaks at 14.40°, 32.76°, 39.55°, 49.68°, 58.26°, and 60.28°. The presence of crystalline phases corresponding to MoS_2 and f-BN is confirmed by the observed diffraction peaks. Specifically, the prominent peak at 14.40° is attributed to the (002) plane of the hexagonal MoS_2, consistent with the standard JCPDS card no. 37-1492. The remaining peaks at 32.76°, 39.55°, 49.68°, 58.26°, and 60.28° are indexed to the (100), (103), (105), (110), and (112) planes of MoS_2, respectively. The composite's high crystallinity, which

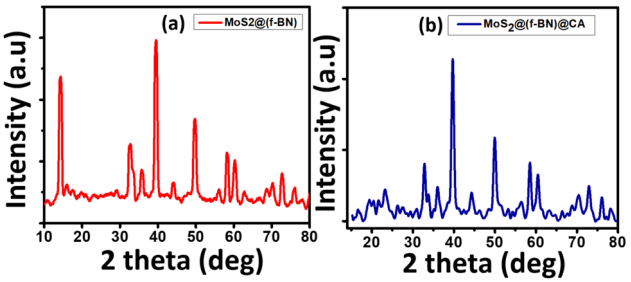

Fig. 1 XRD structures of (a) MoS_2@(f-BN) and (b) MoS_2@(f-BN)@CA.

suggests a well-ordered structure, is indicated by the sharp and distinct peaks. Additionally, the peak's sharpness suggests a manageable crystalline size, emphasizing the synthetic materials' structural integrity. The total peak intensity has decreased, according to the XRD patterns in Fig. 1b. Furthermore, minor adjustments in peak location imply that the lattice strain and the interaction between the composite components may have changed slightly as a result of the addition of cellulose acetate (CA). The appearance of a distinctive peak at 23.08°,[12] which is ascribed to the cellulose acetate component, indicates the presence of a new phase. This broad peak partially masks the expected signal for the (002) plane of f-BN (JCPDS no. 34-0421). The addition of CA probably modifies the stacking and distribution of BN in the composite, resulting in a decrease in the intensity of its BN peak because the newly formed phases partially mask BN peaks upon interaction with CA.

For CA, MoS_2@f-BN, and MoS_2@(f-BN)@CA, the average crystalline size was estimated using the Scherrer equation. The following is the expression for the equation:

$$D = \frac{K\lambda}{\beta \cos\theta} \quad (2)$$

The corresponding sizes of MoS_2@f-BN and MoS_2@(f-BN)@CA are 441.6 Å and 362.8 Å. The strain values, as determined by the Williamson–Hall (W–H) plot method, were 0.28101, 0.11945, and 0.00505 (Fig. 2). As the composite forms, there is a discernible pattern of diminishing strain. The structural interactions between the materials in the composite are probably what caused this decrease in strain. The reduced strain values imply that the addition of CA has enhanced the material's mechanical integrity and stability.[13] Additionally, it is clear that CA strengthens the bonds or interactions between the various components of the composite. By distributing stress more uniformly across the material, these interactions lessen the concentrations of localized strain.[14]

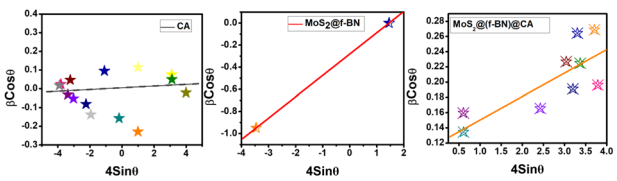

Fig. 2 Williamson–Hall plot of CA, MoS_2@(f-BN) and MoS_2@(f-BN)@CA.

© 2026 The Author(s). Published by the Royal Society of Chemistry

Open Access Article. Published on 19 December 2025. Downloaded on 4/5/2026 8:17:09 PM.
This article is licensed under a Creative Commons Attribution-NonCommercial 3.0 Unported Licence.

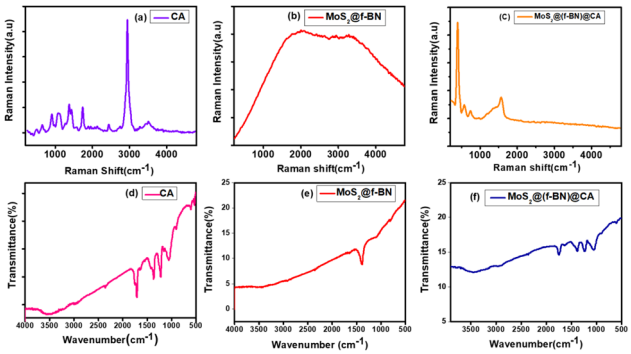

Fig. 3 Raman spectrum of (a) CA, (b) MoS_2@(f-BN), and (c) MoS_2@(f-BN)@CA; FTIR spectrum of (d) CA, (e) MoS_2@(f-BN) and (f) MoS_2@(f-BN)@CA.

The Raman spectra (Fig. 3) offer compelling evidence for the successful integration and strong interfacial coupling within the MoS_2@(f-BN)@CA composite. The presence of the polymer matrix is confirmed by characteristic Cellulose Acetate (CA) vibrational modes, including low-intensity peaks in the 1000–1800 cm^{-1} range (representing skeletal and functional group vibrations like C=O) and a definitive sharp peak at 2939 cm^{-1} (representing C–H stretching).[15] The layered material is identified by the prominent MoS_2 A_{1g} mode at 386 cm^{-1} (representing out-of-plane S vibrations). The observation of this single peak, with the E_{2g} mode (383 cm^{-1}) overlapping or suppressed, is indicative of a few-layer structure. Furthermore, the composite features a peak at 1562 cm^{-1}, assigned to the G band of sp^2 carbon, which confirms the incorporation of carbonaceous structures arising from the functionalized Boron Nitride (f-BN). Crucially, the redshift of the MoS_2 A_{1g} (representing S vibrations) peak to 386 cm^{-1} (representing S atom out-of-plane vibrations)[16] relative to the MoS_2@f-BN precursor indicates a profound modification of the MoS_2 vibrational environment. This shift is primarily attributed to tensile strain induced by the polymer matrix upon solidification and robust interfacial electronic coupling between the MoS_2 and the CA, suggesting a softening of the Mo–S bonds.

This confirms that the integration involves strong non-covalent or mechanical interaction, essential for synergy. Regarding defects, although the D band (1350 cm^{-1}) is obscured by CA peaks, the successful functionalized nature of the BN dictates the presence of structural defects, implying an I_D/I_G ratio greater than zero. This confirms the disorder and edge defects necessary in the carbonaceous component for effective anchoring and interaction with the other materials. The Raman data successfully validate the composite structure, confirm the strong interfacial coupling *via* the observed peak shift, and provide evidence of the structural disorder/functionalization required for an integrated system. An important analytical technique for identifying the existence of functional groups and enhancing the interactions between various components in composite materials is Fourier Transform Infrared (FTIR) spectroscopy. The FTIR spectra of CA, MoS_2@f-BN, and MoS_2@(f-BN)@CA are displayed in Fig. 3d–f. The range of the CA transmittance spectrum is 4000 cm^{-1} to 500 cm^{-1}. The C=O stretching of acetate ester groups is represented by a clear adsorption band that emerges at 1715.12 cm^{-1}.[17] Furthermore, the presence of acetate functions is reinforced by the symmetric deformation of the C–H bond in methyl ($-CH_3$) groups, which is responsible for the peak at 1369.94 cm^{-1}. The structural integrity of cellulose acetate is confirmed by the peak at 1226.8 cm^{-1}, which is linked to C–O stretching, and the noteworthy peak at 1053.53 cm^{-1}, which is related to C–O–C stretching. Fig. 3e shows a prominent absorption band at 1386.7 cm^{-1}, which is usually attributed to in-plane stretching vibrations of B–N bonds in *h*-BN.[18] The most compelling evidence for successful cetyl alcohol grafting lies in the 2800–3000 cm^{-1} region. In this spectrum (Fig. 3e), the appearance of new, distinct, high-wavenumber bands is observed. These peaks are assigned to the C–H asymmetric (2920 cm^{-1}) and symmetric (2850 cm^{-1}) stretching vibrations of the long aliphatic chain (C_{16}) of the cetyl alcohol molecule. Since these peaks are not characteristic of pristine MoS_2 or unfunctionalized BN, their clear presence in the (f-BN)@MoS_2 composite spectroscopically confirms the successful grafting of the cetyl alcohol moiety onto the BN surface. This functionalization is paramount as it enhances the dispersibility and dictates the subsequent strong interfacial coupling with the MoS_2 sheets and the final CA polymer matrix. Strong interfacial interactions are indicated by the combined features from both CA and MoS_2@f-BN in Fig. 3f, which show observable peak shifts and intensity fluctuations. Small variations in the C=O stretching peak at 1746 cm^{-1} point to hydrogen bonding interactions between the MoS_2@f-BN filler and CA. Possible coordination interactions or physical adsorption of CA onto the filler surface are indicated by the presence of the characteristic peak of MoS_2 and B–N, which has been slightly displaced. Strong interfacial contacts between the polymer and the nanofiller are seen in the FTIR measurement, which validates the successful incorporation of MoS_2@f-BN into the matrix.[19]

The optical characteristics and adsorption peaks have been identified through analysis of UV-visible spectra. The bandgap energy and electronic transitions of the materials are revealed by the absorbance spectra. There is a prominent adsorption peak at 218 nm in the CA spectra (Fig. 4a). This is equivalent to

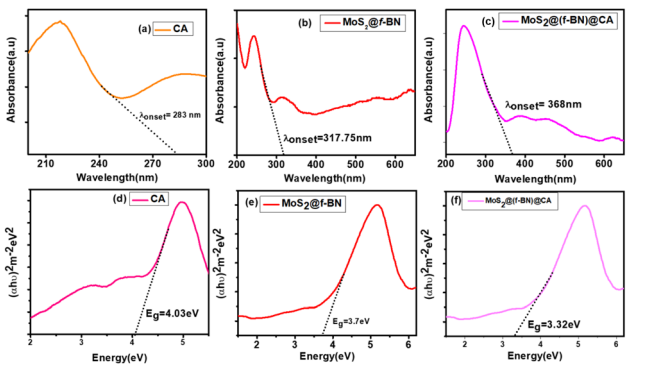

Fig. 4 UV-vis spectrum of (a) CA, (b) MoS_2@(f-BN) and (c) MoS_2@(f-BN)@CA; Tauc plot of (d) CA, (e) MoS_2@(f-BN) and (f) MoS_2@(f-BN)@CA.

Open Access Article. Published on 19 December 2025. Downloaded on 4/5/2026 8:17:09 PM. This article is licensed under a Creative Commons Attribution-NonCommercial 3.0 Unported Licence.

the polymer's carbonyl groups or conjugated systems' π–π* transition.[20] The shift from the highest occupied molecular orbital (HOMO) to the lowest unoccupied molecular orbital (LUMO) is represented by the measured offset wavelength at 283 nm (Fig. 4b and c). CA is an insulating material having restricted electron mobility in optoelectronic applications, as indicated by its predicted bandgap of 4.3 eV. The bandgap of MoS_2@f-BN's UV-visible spectrum is 3.91 eV. The MoS_2@f-BN composite exhibits a lower bandgap, indicating substantial electronic interactions between MoS_2 and BN, even though BN has a high intrinsic bandgap of 5.9 eV.[21] Incorporating MoS_2, a transition metal dichalcogenide with a reduced bandgap of 1.2 eV,[22] significantly changes the composite's electronic structure. By changing the density of states, the hybridization narrows the bandgap. Because MoS_2 has a comparatively larger dielectric constant than BN, it alters the hybrid material's dielectric constant, which impacts the Coulomb interactions between charge carriers.[23] A smaller effective bandgap results from this yield's decreased exciton binding energy, which moves the adsorption edge towards lower energies and modifies the electrical band structure. With an adsorption peak at 368 nm and a bandgap reduction to 3.3 eV, the composite of MoS_2@(f-BN)@CA exhibits an additional redshift, suggesting enhanced light adsorption and electronic conduction capabilities. The bandgap energy steadily declines from

4.3 eV (CA) → 3.91 eV (MoS_2@f-BN) → 3.3 eV (MoS_2@(f-BN)@CA)

which implies that adding MoS_2 to CA results in the creation of a material with better optical and electrical characteristics.

Tauc plots, which are based on the Tauc relation derived from the adsorption coefficient and photon energy, can be used to identify a material's optical bandgap.[24]

The Tauc equation is

$$(\alpha h\nu)^n = A(h\nu - E_g) \quad (3)$$

where α is the absorption coefficient, $h\nu$ represents the photon energy, E_g is the optical bandgap energy, A is a constant, and $n = 1/2$ for direct allowed transitions and $n = 2$ for indirect allowed transitions.

From Fig. 4 and Table 1, the Tauc bandgap has close agreement with the UV-vis determined values. It's evident that the bandgap decreases with the formation of composites. This reduction confirms that the incorporation of MoS_2 and f-BN into the CA matrix promotes enhanced electronic interactions and the introduction of defect states, both of which contribute to bandgap narrowing. The composite with the lowest bandgap, 3.32 eV, is the best because it shows improved optical absorption and the promise for improved performance in light-driven applications. Due to its enhanced optical absorption and potential for better performance in light-driven applications, the composite with the lowest bandgap, 3.32 eV, is the best. By adding MoS_2, a substance with a tiny bandgap, additional energy levels are added to the composite's band structure. The total bandgap energy can be reduced thanks to these additional states. An increased capacity to absorb visible light, which is essential for raising photocatalytic effectiveness, is suggested by the observed bandgap reduction. The composite's CA component serves as a porous and flexible support. By placing pollutants close to the active areas for degradation, this porous structure makes it easier for them to be adsorbed. It is also clear that the CA offers a porous support for pollutant adsorption, the f-BN makes charge separation and transport easier, and MoS_2 offers active sites for photocatalysis and improves light absorption.[25] This synergistic combination greatly enhances the overall water purification efficacy as compared to the separate components.

The optical characteristics of BNNS, MoS_2, and MoS_2@(f-BN)@CA are displayed in the supplied photoluminescence (PL) spectra. There are new characteristics in the spectrum of the composite PL that point to a changed electronic structure. Fig. 5a and b shows that the composite's bandgap (3.3 eV) is higher than that of MoS_2 but lower than that of BNNS, indicating charge transfer and hybridization effects. It is a transition metal dichalcogenide (TMD) with a direct bandgap of 1.9 eV. When MoS_2 is added, electrons can move between the MoS_2 and BNNS surfaces, creating an effective heterojunction. This happens when boron nitride with a greater bandgap is applied. The energy levels are modulated by the interfacial dipole effect from MoS_2 to BN, which shifts the Fermi level and reduces the optical bandgap. In addition to stabilizing excitations and further altering the electronic structure, CA offers more charge-trapping sites. Defect states and surface functional groups that contribute to the mid-gap energy states are enhanced when CA is present. The composite's potential for photocatalytic applications is increased by the reduction in bandgap, which suggests that it can absorb light in a wider range (UV-vis). Fig. 5c shows the thermogravimetric curve of the MoS_2@(f-BN)@CA composite that was recorded in a nitrogen atmosphere at a heating rate of 20 °C min^{-1}. TGA was carried out to evaluate the composite's heat stability and deterioration trends. The thermogram shows a multi-step deterioration process, which is a sign of the different thermal stabilities of the

Table 1 Bandgap determination from the UV-vis spectrum and Tauc plot

Sample code	UV-vis spectrum E_g (eV)	Tauc plot E_g (eV)
CA	4.3	4.02
MoS_2@f-BN	3.91	3.7
MoS_2@f-BN@CA	3.3	3.32

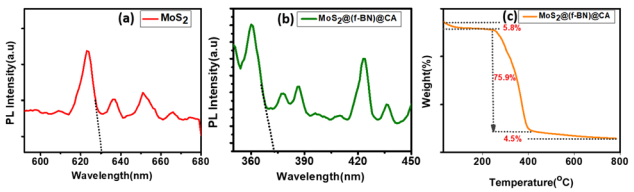

Fig. 5 PL spectra of (a) BNNS, (b) MoS_2 and (c) MoS_2@(f-BN)@CA; (c) TGA of the MoS_2@(f-BN)@CA composite.

© 2026 The Author(s). Published by the Royal Society of Chemistry

Open Access Article. Published on 19 December 2025. Downloaded on 4/5/2026 8:17:09 PM. This article is licensed under a Creative Commons Attribution-NonCommercial 3.0 Unported Licence.

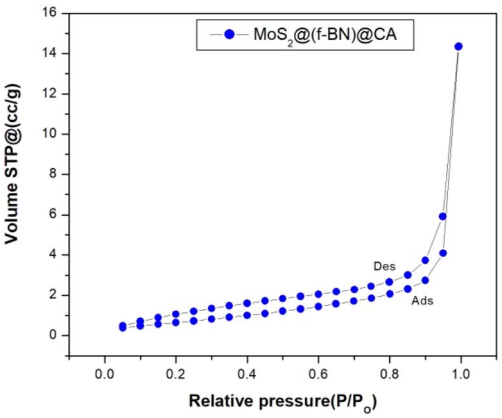

Fig. 6 BET analysis of the MoS_2@(f-BN)@CA composite.

constituent parts of the composite. When it comes to thermal stability, CA is the least stable compared to MoS_2 and BN. Mass losses of 5.8%, 75.9%, and 4.2% are shown in Fig. 5, along with a degradation onset temperature of 249 °C. The first weight loss is ascribed to the elimination of the sample's remaining solvent molecules, adsorbed moisture, and other volatile contaminants. Degradation of any highly labile fractions of the CA components with reduced heat stability is also included. Between 249 °C and 400 °C, the greatest weight loss of 75.9% takes place. The thermal breakdown of the cellulose acetate (CA) matrix is attributed to the significant mass loss event. In this temperature range, CA is known to experience chain scission and depolymerization.[26] A residual weight of 4.5% is left over at temperatures above 600 °C, which is explained by the existence of inorganic components like f-BN and MoS_2, which are thermally stable by nature. The residual weight shows that the addition of MoS_2 and f-BN improves the composite's overall thermal stability, especially at higher temperatures.

Fig. 6 displays the nitrogen adsorption–desorption isotherm for the MoS_2@(f-BN)@CA composite material, which is fundamental to characterizing its porous structure and surface properties from BET analysis. A distinct hysteresis loop is present, defined by the separation between the Adsorption (Ads) and Desorption (Des) branches, confirming the material's porous nature.[27] This loop initiates at a moderate relative pressure and remains open up to $P/P_0 \sim 1.0$. The shape of the loop appears to be a mixed type, resembling H_3 or H_4 hysteresis,[28] which is commonly observed for materials made of aggregates or agglomerates of plate-like particles, consistent with the layered structure of MoS_2 and BN.

The total adsorbed volume at the highest relative pressure ($P/P_0 \sim 0.99$), which reaches approximately 14 $cm^3\ g^{-1}$ in this plot, is used to estimate the total pore volume of the material. The high magnitude of this volume indicates a highly porous structure, suggesting that the CA matrix and the MoS_2/f-BN integration successfully created a robust, accessible porous network.

Monolayer adsorbed gas volume (V_m) is derived

$$V_m = \frac{1}{(\text{slope} + \text{intercept})} \quad (4)$$

$$S_{BET} = \frac{V_m \times N \times A}{V_{molar}} \quad (5)$$

where V_m is the monolayer adsorbed gas volume; N the Avogadro number; A the cross-sectional area of the nitrogen molecule; V_{molar} the molar volume of adsorbed gas; and S_{BET} the specific surface area.

The BET specific surface area of the MoS_2@(f-BN)@CA is calculated using the above equations and is found to be 230 $m^2\ g^{-1}$. The significant increase in the S_{BET} compared to its individual components, MoS_2 and BN, is a common and highly desired phenomenon in composite material design for photodegradation.[29] MoS_2 typically has a specific surface area that can range from approximately 5 $m^2\ g^{-1}$ to over 70 $m^2\ g^{-1}$ depending on its morphology (*e.g.*, bulk, flower-like, or exfoliated nanosheets) and preparation method. Similarly, bulk hexagonal Boron Nitride (*h*-BN) is known for its low surface area. The synergistic combination of these two-dimensional (2D) materials into a composite structure often results in exfoliation and prevention of restacking of the individual layers, leading to the formation of a hierarchical, porous structure or a highly dispersed configuration. This increased surface area provides significantly more active sites for the adsorption of pollutant molecules, which is the crucial initial step in photocatalytic degradation. A larger surface area, as confirmed by the S_{BET} value of 230 $m^2\ g^{-1}$, directly translates to enhanced adsorption capacity and greater exposure of the catalyst's active edges,

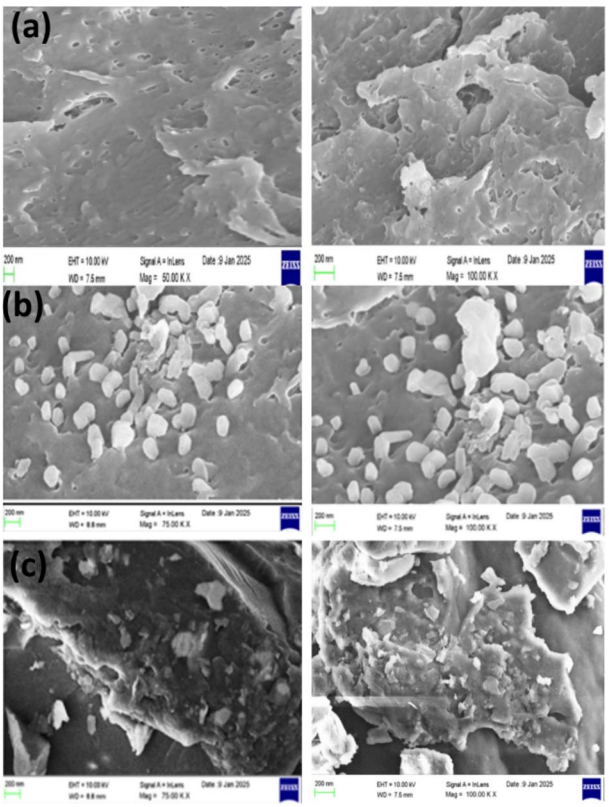

Fig. 7 FESEM images of (a) CA, (b) MoS_2@(f-BN) and (c) MoS_2@(f-BN)@CA.

Open Access Article. Published on 19 December 2025. Downloaded on 4/5/2026 8:17:09 PM.
This article is licensed under a Creative Commons Attribution-NonCommercial 3.0 Unported Licence.

ultimately boosting the efficiency and kinetics of the photodegradation process.[30]

Fig. 7 shows images obtained using FE-SEM, a potent imaging method that may be utilized to analyze the material's surface morphology and phase distribution properties at incredibly high resolutions. Cellulose acetate's SEM micrographs (Fig. 7a) show a diverse surface morphology with rough, uneven textures. Potential phase separation is indicated by the surface's apparent porosity and scattered voids. A non-uniform distribution of polymer chains was suggested by the microstructure, which showed fibrillar features and interconnected domains. SEM pictures in Fig. 7b demonstrated a consistent distribution of MoS_2 particles in the matrix of functionalized boron nitride (f-BN). The MoS_2 particles adhered to the f-BN framework and showed a flake-like or layered structure. Because of the functionalization, agglomerated clusters indicated significant interfacial contacts. Surface granular features suggested the formation of a heterostructure, which could improve mechanical and thermal properties. Effective deposition is shown by the comparatively equal distribution of MoS_2 across f-BN, which is essential for optimizing sophisticated filtration systems. Fig. 7c shows the MoS_2@(f-BN)@CA composite's SEM picture. An uneven and rough surface is seen in the picture, indicating that the composite's constituent parts are distributed uniformly. Adsorption and filtration are two uses that benefit from the porous morphology.[31] The flake-like, layered pattern that was visible at higher magnification was consistent with 2D materials such as f-BN and MoS_2. Surface roughness, which was previously noted, demonstrated how interwoven the composite structure was.

The elemental composition of the synthesized composite was investigated using Energy-Dispersive X-ray Spectroscopy (EDS). The spectrum, displayed in Fig. 8, reveals prominent signals for Mo and S, which are the characteristic elements of the MoS_2 two-dimensional material. Concurrently, high-intensity peaks for carbon and oxygen are observed, originating primarily from the cellulose acetate polymer matrix and the cetyl alcohol functionalization agent. The elemental composition of the hybrid material is confirmed by the presence of characteristic energy peaks for Mo (2.2 wt%) and S (3.7 wt%), originating from the MoS_2 component, alongside peaks for boron (B, 25.1 wt%) and nitrogen (N, 21.6 wt%), which are indicative of the BN material.

Furthermore, the foundational matrix and functionalization are confirmed by the strong signals for C and O, which are the primary constituents of the cellulose acetate polymer backbone and the cetyl alcohol. The uniform and distinct distribution of Mo, S, B, and N across the analyzed area, as observed in the elemental maps, validates the effective incorporation and dispersion of both two-dimensional (2D) materials throughout the composite structure, rather than forming large agglomerates.[32] The presence of a strong C signal from the polymer, along with the elements of the 2D materials and the functionalizing agent, unequivocally confirms the formation of a multi-component hybrid composite. The EDS data clearly shows that the B and N, which make up the BN material, are located in the same areas as the long chains of carbon from the cetyl alcohol. This co-localization strongly indicates that the cetyl alcohol successfully functionalized the *h*-BN. This surface modification is critical because it allowed the BN to be evenly and smoothly distributed throughout the polymer.[33] A good, uniform distribution is essential for the overall stability of the hybrid system and its proper integration within the CA matrix.

The colloidal stability and surface chemistry of the composite were critically evaluated through zeta potential measurements (Fig. 9). The *h*-BN and MoS_2 nanosheets exhibit an anionic surface charge in neutral aqueous media, often reporting values in the −20 mV to −50 mV range due to surface hydroxyl groups or sulfur vacancies, respectively, or sometimes near 0 mV under specific ionic conditions.[34,35] The final composite displayed a mean zeta potential of +21 mV in the testing medium. This dramatic shift of at least 21 mV into the positive domain is the key evidence confirming the effectiveness of the *h*-BN functionalization using cetyl alcohol. This successful grafting or association of cetyl groups has fundamentally modified the electric double layer of the particles. The incorporation of these long-chain fatty moieties, possibly facilitated by a cationic reaction intermediary, successfully masked the native anionic sites and introduced a net cationic character to the composite surface. Furthermore, the magnitude of +21 mV falls within the range generally associated with moderate to good colloidal stability, indicating that the successful surface modification not only changed the charge polarity but also enhanced the electrostatic repulsion between the composite particles.[36] This increase in

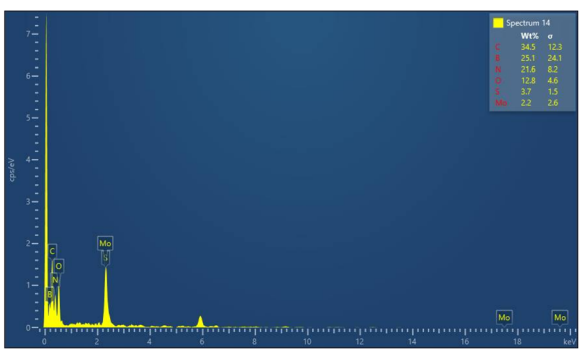

Fig. 8 EDS mapping of MoS_2@(f-BN)@CA.

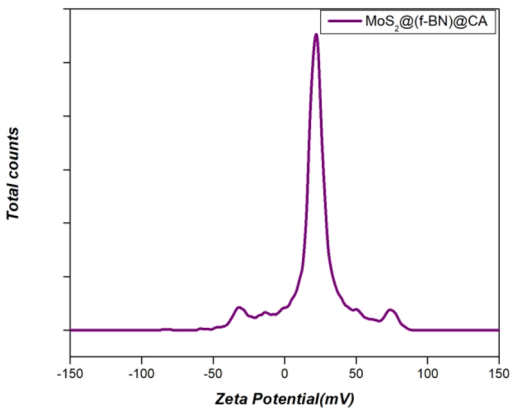

Fig. 9 Zeta potential distribution curve of MoS_2@(f-BN)@CA.

© 2026 The Author(s). Published by the Royal Society of Chemistry

Open Access Article. Published on 19 December 2025. Downloaded on 4/5/2026 8:17:09 PM.
This article is licensed under a Creative Commons Attribution-NonCommercial 3.0 Unported Licence.

repulsion is crucial for maintaining a well-dispersed, stable suspension, which is necessary for effective processing and integration into the cellulose matrix.

4 Photodegradation of crystal violet

4.1 Effect of irradiation time

The photocatalytic activity of the MoS_2@(f-BN)@CA composite regarding crystal violet (CV) dye breakdown was carefully assessed, controlling artificial sunlight contact. In a typical experiment, the composite (0.2 g) was put into 100 mL of a 5 mg per L CV solution, with the temperature remaining constant. There were no temperature fluctuations. Fig. 10a depicts the percentage of CV eliminated over a time frame, from 20 to 120 minutes. The degradation process began with a substantial 65% elimination and a constant rise when irradiation times were longer. After a duration of two hours, the removal efficiency exceeded 86%, which demonstrated the composite's prominent photocatalytic capacity. The outstanding final rate of decline shows that the stimulus maintained how well it worked during the research.[37] The noted great efficacy of breakdown after two hours suggests the MoS_2@(f-BN)@CA mix is a helpful photocatalyst for CV elimination. The steady action throughout the study indicates proper stimulus stability and a chance for reapplication. The special process associated with photocreated charge carriers and the clearly cooperative effect of f-BN and CA considerably add to the noticeably improved photocatalytic ability of the combination.[38]

4.2 Effect of pH

The degradation of CV dye with respect to different pH values was monitored. A CV solution of 5 mg L^{-1} was created, and its pH was set to a value between 2 and 10 by adding either 1 M HCl or 1 M NaOH. Before changing the pH of the CV solution, its initial absorbance was calculated at the wavelength of 664 nm using UV-vis. The results (Fig. 10b) suggest that the composite showed optimum CV degrading efficiency at approximately pH 6 and achieved 50% degradation under the test conditions.

At low pH values (around 2), the surface of the MoS_2@(f-BN)@CA composite photocatalyst is expected to have a stronger positive charge due to the capture of protons. The pH of a solution can greatly affect the surface charge of the photocatalyst and the dissociation state of the dye molecules. A cationic dye, CV, is positively charged when in solution. The decrease in adsorption efficiency is likely due to electrostatic repulsion between the cationic CV molecules and the catalyst surface, contributing to lower degradation efficiency.

The perfect physisorption plays an important role in the successful degradation of dye molecules photocatalytically, as it enables the location of molecules close to the active sites, from where charge carriers engaged in the photogeneration process can start the degradation.[39] Near pH 6, the interaction between the surface charge of the composite and the ionization state of CV is thought to be favorable for adsorption and subsequent photocatalytic decomposition. The 50% degradation efficiency observed at pH 6 indicates that, under these intensive conditions, the composite exhibits an optimal balance of surface charge, ionization of CV, and sufficient photocatalytically active degradation reactive species.[40]

4.3 Effect of concentration

To explore the degradation process, the initial crystal violet dye concentration was varied from 1 mg L^{-1} to 5 mg L^{-1}. Each experiment began with adding 0.2 g of MoS_2@(f-BN)@CA composite to 100 mL of CV solution. The relation between initial dye concentration and the percentage of degradation has been developed. This can be seen from the result (Fig. 10c).

The provided graph illustrates the relationship between the initial dye concentration of crystal violet and the percentage removal efficiency using the MoS_2@(f-BN)@CA composite. The data clearly show a monotonic decrease in the removal efficiency as the initial dye concentration increases from 1 mg L^{-1} to 5 mg L^{-1}. Specifically, the removal efficiency drops significantly, starting near 79% at 1 mg L^{-1} and falling to approximately 10% at 5 mg L^{-1}. This trend is consistent with standard photocatalytic kinetics, where increasing the initial substrate concentration leads to a greater number of dye molecules competing for a limited number of active sites and reactive species ($OH^{\bullet}$, $O_2^{-\bullet}$),[41] ultimately resulting in a lower percentage of total molecules being degraded within the experimental time. Furthermore, the higher concentration of dye molecules in the solution can also lead to an increased light screening effect, preventing photons from reaching the catalyst surface and hindering the generation of electron–hole pairs, which further reduces the overall removal efficiency.

4.4 Effect of catalyst dose

The effect of catalyst dosage on CV degradation was tested using 0.1 g to 0.5 g of the MoS_2@(f-BN)@CA composite. As shown in

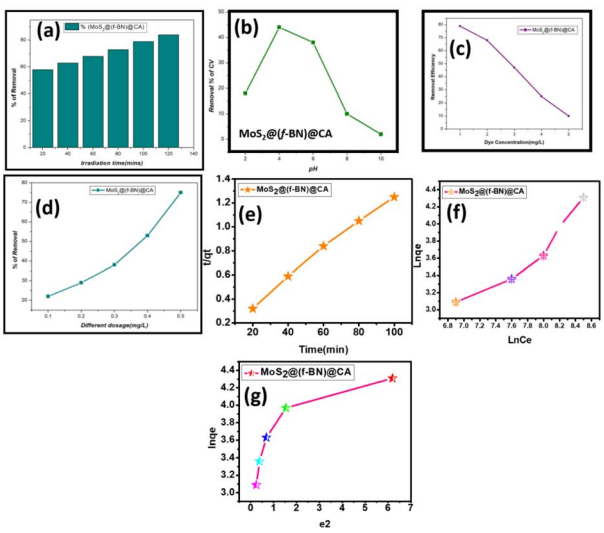

Fig. 10 (a) Bar graph representing the effect of irradiation time, (b) effect of pH on degradation of crystal violet by MoS_2@(f-BN)@CA, (c) effect of dye concentration (CV), (d) influence of catalyst dosage on CV dye; (e) pseudo-second order kinetics-graph between t/q_t and time. (f) Freundlich model isotherm-graph between ln C_e and ln q_e (g). Dubinin–Radushkevich isotherm-graph between ln q_e and e2.

Open Access Article. Published on 19 December 2025. Downloaded on 4/5/2026 8:17:09 PM. This article is licensed under a Creative Commons Attribution-NonCommercial 3.0 Unported Licence.

Fig. 10d, the relationship between catalyst dosage and the CV removal percentage was observed. At 0.1 g, 22% of the dye was removed, and increasing the dosage resulted in a further improvement in removal efficiency, reaching about 53 percent at 0.4 g and 75% at 0.5 g. These findings unequivocally show that catalyst dose and CV deterioration are positively correlated. More surface area and active sites are available for the adsorption and catalytic breakdown of CV at larger catalyst doses. The mechanism entails the photocatalytic degradation process after CV molecules are adsorbed onto the composite's surface. When exposed to light, the MoS_2 component serves as the main photocatalyst, producing electron–hole pairs. The disintegration of the adsorbed CV molecules is caused by these charge carriers migrating to the composite's surface and engaging in redox reactions with them. It is probable that the f-BN component contributes to improving charge separation and offering more active sites. By providing a porous structure that promotes dye adsorption, the CA matrix might be beneficial.[42] The significance of catalyst dosage in optimizing the photocatalytic process is demonstrated by the rise in removal efficiency from 22% at 0.1 g to 75% at 0.5 g. More active sites are provided by the increased dosage, which leads to a higher number of CV molecules being degraded.

The individual materials-pure BN nanosheets, the CA polymer matrix, and pristine MoS_2-exhibited negligible or poor degradation activity toward Crystal Violet (CV) dye. Pure MoS_2 achieved ~20%.[43] Specifically, the lack of a suitable band structure meant CA showed minimal efficiency beyond minor physical adsorption, and the wide bandgap of BN resulted in virtually inert performance, confirming their roles as structural supports rather than primary photocatalysts.[44,45] While the binary MoS_2/BN composite demonstrated improved activity over single components due to the initial formation of a heterojunction, its performance remained moderate (~70–75%) as its efficiency was limited by inefficient interfacial charge transfer and difficulty in recovery.[46] In an effort to advance water treatment technologies, recent studies have investigated the effectiveness of MoS_2/BN/rGO ternary nanocomposites for treating organic dye-contaminated water, specifically focusing on their performance in Oxygen Evolution Reaction (OER) and Hydrogen Evolution Reaction (HER) processes. In stark contrast, the fully integrated MoS_2@(f-BN)@CA ternary composite achieved a high degradation efficiency of 86%. This remarkable performance differential rigorously quantifies the pronounced synergy generated by our architecture, demonstrating that the functionalized f-BN/MoS_2 heterojunction combined with the CA matrix is essential to unlock the high-efficiency potential, validating the rationale behind our complex material design.

4.5 Adsorption isotherm and kinetics

Adsorption isotherm models are essential for comprehending how adsorbate molecules interact with the photocatalyst surface. Adsorption is a crucial initial step that affects the overall degradation efficiency in the photocatalytic breakdown of dyes like crystal violet. Because of its special physicochemical characteristics, the MoS_2@(f-BN)@CA composite is an effective adsorbent and photocatalyst for the elimination of CV. With a contact time of 120 minutes and 25 °C, the highest adsorption effectiveness of 86% was attained. The primary adsorption mechanism, whether it be energy-dependent adsorption (Temkin), multilayer adsorption (Freundlich), monolayer adsorption (Langmuir), Dublin–Radushkevich (D–R), or Harkins–Jura isotherm, can be identified by fitting experimental data to isotherm models. The Freundlich isotherm provides the best description of the adsorption behavior of the functionalized Boron Nitride (f-BN)/MoS_2/Cellulose Acetate (CA) composite. It shows a heterogeneous adsorption surface, where adsorption takes place at various energy levels instead of forming a homogeneous monolayer. Photodegradation of CV using the MoS_2@(f-BN)@CA material as a photocatalyst under sunlight is shown in Scheme 1. Adsorption on a heterogeneous surface with non-uniform adsorption sites and multilayer adsorption is described empirically by the Freundlich isotherm.[47] Mathematically, it is represented as:

$$q_e = K_F C_e^{1/n} \quad (6)$$

where q_e is the amount of adsorbate per unit mass of the composite, C_e is the equilibrium concentration of the pollutant, K_F is the Freundlich constant (indicating adsorption capacity), and $1/n$ is the heterogeneity factor (values between 0 and 1 indicate favorable adsorption).

The Freundlich model over Langmuir is supported by the $\ln(q_e)$ *vs.* $\ln(C_e)$ graph (Fig. 10f), which displays a comparatively linear trend and indicates that adsorption takes place on sites with different binding strengths. Because the Langmuir adsorption graph does not exhibit a perfect linear relationship, the composite does not adhere to Langmuir adsorption, which is based on the assumption of a single, uniform layer of adsorbate on the surface. For wastewater treatment applications, the Freundlich fit suggests that adsorption is advantageous and increases with pollutant concentration.

Instead of a single, homogeneous monolayer, multilayer adsorption results from the existence of distinct adsorption sites with differing affinities caused by the Freundlich model. Prior to photodegradation, pollutants are better retained thanks to the multilayer effect. Because of the porosity design created by the cellulose acetate (CA) matrix, contaminants can become trapped inside the network. Furthermore, the adsorption of

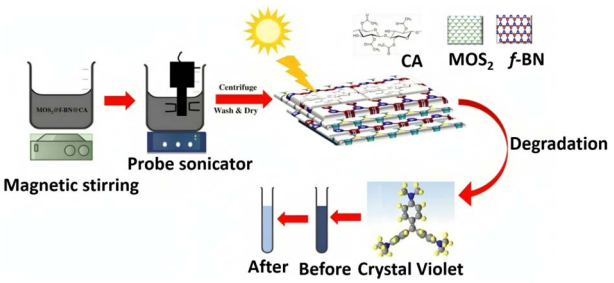

Scheme 1 Photodegradation of crystal violet using the MoS_2@(f-BN)@CA composite as a photocatalyst under sunlight.

© 2026 The Author(s). Published by the Royal Society of Chemistry

Open Access Article. Published on 19 December 2025. Downloaded on 4/5/2026 8:17:09 PM.
This article is licensed under a Creative Commons Attribution-NonCommercial 3.0 Unported Licence.

nonpolar molecules is supported by weak van der Waals forces. Whether adsorption is physisorption or chemisorption is also determined by the Radushkevich–Dubinin (D–R) isotherm (Fig. 10g). Both chemisorption (stronger chemical interactions) and physisorption (weak van der Waals forces) are involved in the adsorption mechanism. By providing active edge sites and flaws, MoS_2 and functionalized BN aid in the adsorption process and improve pollutant binding. Because of its porous nature, cellulose acetate (CA) increases the surface area and diffusion channels that pollutants can use. In addition to guaranteeing adsorbate mobility, which is necessary for desorption and reusability, the hybrid interaction enables efficient pollutant capture. Following adsorption, exposure to light triggers photodegradation. As a photocatalyst, MoS_2, a transition metal dichalcogenide (TMD), creates electron–hole pairs by absorbing light. By preventing charge recombination, f-BN enables the electrons and holes to efficiently break down adsorbed contaminants. As a result, organic pollutants and colors decompose into non-toxic byproducts. The composite may work especially well at increasing pollutant levels because the Freundlich model indicates that adsorption capacity rises with pollutant concentration. Because of this characteristic, it is perfect for treating wastewater that contains pollutants in different amounts. Because deposited contaminants can decompose in the presence of light, releasing active sites for additional adsorption cycles, the composite's reusability is also improved. From heavy metals to organic poisons, the heterogeneous surface guarantees the removal of a wide range of contaminants.

The composite is an eco-friendly water treatment option because of its non-toxic f-BN/MoS_2 structure and biodegradable components (CA). The plot's nonlinearity indicates that physical interactions are also a part of the adsorption mechanism, in addition to chemical ones.

According to the interpretation of the Freundlich isotherm, the adsorption process is favorable, and the slope $(1/n)$ is 0.7465. Additionally, $N = 1.3396$ validates the heterogeneous character of the materials. Furthermore, K_f of 0.3424 and R^2 of 0.9143 indicate good correlation with and great adherence to the Freundlich model in the composite. The slow rise in q_e as C_e increases indicates that the adsorption sites differ in energy levels rather than being similar. Surface heterogeneity may result from different pore structures, surface roughness, or functional groups, all of which can affect adsorption efficiency. The correlation coefficient (R^2) is the primary determinant of a kinetic model's capability for characterizing the degradation process. Adsorption in which chemisorption, not simply diffusion, controls the rate is described by the pseudo-second order kinetic model.[48]

It is denoted by the equation

$$\frac{dq}{dt} = k_2(q_e - q_t)^2 \quad (7)$$

where q_t is the adsorption capacity at time t, q_e is the equilibrium adsorption capacity, and k_2 is the pseudo-second-order rate constant.

According to the model, chemical bonding predominates, and the adsorption rate is proportional to the square of the accessible sites.

The high R^2 value of 0.9956 for the MoS_2@(f-BN)@CA composite suggests that chemisorption is the main process, and the perfect fit to the experimental data validates pseudo-second-order. This implies that chemisorption, in which stronger forces like covalent bonding, charge transfer, or surface reaction mechanisms interact with the adsorbate on the composite surface, dominates the adsorption mechanism. It may be concluded that the photodegradation process of our composite is probably controlled by chemical interactions rather than straightforward physical adsorption because the pseudo-second-order model fits the data considerably better (Fig. 10e).

Consequently, the best alternative to explaining the dynamics of this system is the pseudo-second-order model. The main process is chemisorption, and the adsorption rate is proportional to the square of the available sites. The heterogeneous adsorption surface shown by the Freundlich isotherm verifies the presence of many active site types in BN, MoS_2, and cellulose acetate. This is corroborated by the pseudo-second order model, which shows that adsorption requires strong chemical bonds at these sites in addition to being a physical process. Freundlich prediction of multilayer adsorption is consistent with the pseudo-second-order model since chemisorption can take place in several layers, as indicated by the pseudo-second order kinetics (t/q_t against time) graph, particularly in materials with nanostructures like MoS_2 and BN. The functionalized composite has active sites based on hydroxyl, sulphur, and boron that have significant interactions with the adsorbate through electrostatic forces, π–π interactions, and hydrogen bonds. The ease of adsorption is indicated by the Freundlich isotherm constant, n. Strong surface interactions are implied if $1/n$ is less than 1.[49] The notion that adsorption efficiency is determined by chemical forces is supported by the pseudo-second-order model, which implies that these interactions are rate-controlling. By improving surface functionality, adsorption capacity, and chemical affinity, the combination of BN, MoS_2, and cellulose acetate makes this composite extremely effective for environmental remediation.

5 Conclusion

A novel MoS_2@(f-BN)@CA composite was successfully synthesized and characterized in this study for the efficient photodegradation of crystal violet (CV) dye. A number of important aspects contributed to the composite's increased photocatalytic activity. A smaller bandgap of 3.2 eV was verified by the UV study, which allowed for effective light absorption and electron–hole pair formation. The overall photocatalytic effectiveness was increased by improving charge separation and decreasing electron–hole recombination, which was probably made possible by the presence of f-BN in the composite structure. The rationally engineered ternary composite, MoS_2@(f-BN)@CA, achieved a remarkable photocatalytic efficiency of 86% for the degradation of recalcitrant crystal violet (CV) dye under visible

Open Access Article. Published on 19 December 2025. Downloaded on 4/5/2026 8:17:09 PM. This article is licensed under a Creative Commons Attribution-NonCommercial 3.0 Unported Licence.

light, representing a superior performance profile that significantly exceeds previous literature reports on simple polymer-supported MoS_2/(BN) systems. This implies multilayer adsorption and a heterogeneous adsorption surface, both of which are advantageous for the removal of different contaminants. Strong contacts between the CV molecules and the composite surface are suggested by the pseudo-second-order kinetic model, which shows that chemisorption is an important part of the adsorption process. The exceptional specific surface area of 230 $m^2 g^{-1}$, confirmed by BET analysis, demonstrates a synergistic effect within the composite. This drastically enhanced surface area directly supports the material's superior adsorption capacity, providing abundant active sites essential for initiating and boosting the photodegradation kinetics of organic dye pollutants. By offering a porous structure that improves dye adsorption and makes it easier for contaminants to diffuse to the active areas, the CA matrix helps the composite function better. MoS_2, f-BN, and CA work in concert within the composite structure to improve surface functioning, adsorption capacity, and chemical affinity for contaminants. These factors all contribute to the composite structure's exceptional environmental remediation performance. A thorough examination of the composite's optical, electrochemical, structural, and adsorption characteristics, and removal efficiency validates its promise as a wastewater treatment material. In addition to helping to develop cutting-edge materials for environmental remediation and encouraging sustainable water purification methods, the MoS_2@(f-BN)@CA composite's combined adsorption and photocatalytic capabilities provide an effective and sustainable method for removing organic pollutants from water.

Author contributions

S. M. N.: formal analysis, investigation, methodology, writing – original draft, writing – review and editing; B. B.: methodology, project administration, supervision, validation, visualization, writing – review and editing; J. H.: formal analysis; R. R. & A. A. S.: formal analysis, visualization; P. N.: formal analysis, visualization; A. A.: formal analysis, validation; D. M.: validation; A. M.: writing – review and editing.

Conflicts of interest

The authors declare no conflict of interest.

Data availability

The data that support the findings of this study are available from the corresponding author upon reasonable request.

Acknowledgements

The authors would like to express their sincere gratitude to Noorul Islam Centre for Higher Education, Tamil Nadu, for assisting in carrying out this research work. This project is also supported by the Ongoing Research Funding Program (ORF-2026-238), King Saud University, Riyadh, Saudi Arabia.

References

1 F. P. Camargo, P. S. Tonello, A. C. A. Santos and I. C. S. Duarte, Removal of toxic metals from sewage sludge through chemical, physical, and biological treatments—a review, *Water Air Soil Pollut.*, 2016, **227**, 433.
2 X. Bai, W. Chen, B. Wang, T. Sun, B. Wu and Y. Wang, Photocatalytic degradation of some typical antibiotics: recent advances and future outlooks, *Int. J. Mol. Sci.*, 2022, **23**, 8130.
3 Y. Nosaka and A. Y. Nosaka, Generation and detection of reactive oxygen species in photocatalysis, *Chem. Rev.*, 2017, **117**, 11302–11336.
4 R. J. Braham and A. T. Harris, Review of major design and scale-up considerations for solar photocatalytic reactors, *Ind. Eng. Chem. Res.*, 2009, **48**, 8890–8905.
5 X. Li, X. Zheng, Y. Zhen and Y. Liang, Photogenerated carrier-assisted electrocatalysts for efficient water splitting, *Catalysts*, 2023, **13**, 712.
6 S. Hao, X. Zhao, Q. Cheng, Y. Xing, W. Ma, X. Wang, G. Zhao and X. Xu, A Mini Review of the Preparation and Photocatalytic Properties of Two-Dimensional Materials, *Front. Chem.*, 2020, **8**, 582146.
7 A. Vijayan and N. Sandhyarani, Synthesis and characterization of photocatalytic materials, *Photocatalysis*, 2021, **1**, 1–35.
8 V. Takhar and S. Singh, Nanomaterials ROS: a comprehensive review for environmental applications, *Environ. Sci. Nano*, 2025, **12**, 2516–2550.
9 H. Shaghaleh, X. Xu and S. Wang, Current progress in production of biopolymeric materials based on cellulose, cellulose nanofibers, and cellulose derivatives, *RSC Adv.*, 2018, **8**, 825–842.
10 J. Ren and P. Innocenzi, 2D boron nitride heterostructures: recent advances and future challenges, *Small Struct.*, 2021, **2**, 2100068.
11 Z. Yang, Y. Zhou, Z. Feng, X. Rui, T. Zhang and Z. Zhang, A review on Reverse osmosis and nanofiltration membranes for water purification, *Polymers*, 2019, **11**, 1252.
12 S. Yoshitake, T. Suzuki, Y. Miyashita, D. Aoki, Y. Teramoto and Y. Nishio, Nanoincorporation of layered double hydroxides into a miscible blend system of cellulose acetate with poly(acryloyl morpholine), *Carbohydr. Polym.*, 2013, **93**, 331–338.
13 S. Mustapha and Y. Andou, Enhancing Mechanical Properties of Polyurethane with Cellulose Acetate as Chain Extender, *Fibers Polym.*, 2021, **22**, 2112–2118.
14 L. Yao, C. Lee and J. Kim, Electrospun meta-aramid/cellulose acetate and meta-aramid/cellulose composite nanofibers, *Fibers Polym.*, 2011, **12**, 197–206.
15 X. He, X. Liu, B. Nie and D. Song, FTIR and Raman spectroscopy characterization of functional groups in various rank coals, *Fuel*, 2017, **206**, 555–563.

© 2026 The Author(s). Published by the Royal Society of Chemistry

Open Access Article. Published on 19 December 2025. Downloaded on 4/5/2026 8:17:09 PM. This article is licensed under a Creative Commons Attribution-NonCommercial 3.0 Unported Licence.

16 A. P. S. Gaur, S. Sahoo, M. Ahmadi, M. J. F. Guinel, S. K. Gupta, R. Pandey, K. D. Sandwip and R. S. Katiyar, Optical and Vibrational Studies of Partially Edge-Terminated Vertically Aligned Nanocrystalline MoS2 Thin Films, *J. Phys. Chem. C*, 2013, **117**, 26262–26268.
17 J. Dybal, J. Štokr and B. Schneider, C=O Stretching vibrations in Raman and infrared spectra of simple esters, *Collect. Czech. Chem. Commun.*, 1982, **47**, 2027–2036.
18 S. Jäger, K. Bewilogua and C. P. Klages, Infrared spectroscopic investigations on h-BN and mixed h/c-BN thin films, *Thin Solid Films*, 1994, **245**, 50–54.
19 J. Njuguna, K. Pielichowski and S. Desai, Nanofiller-reinforced polymer nanocomposites, *Polym. Adv. Technol.*, 2008, **19**, 947–959.
20 A. Pettignano, A. Charlot and E. Fleury, Carboxyl-functionalized derivatives of carboxymethyl cellulose: towards advanced biomedical applications, *Polym. Rev.*, 2019, **59**, 510–560.
21 J. Wang, F. Ma and M. Sun, Graphene, hexagonal boron nitride, and their heterostructures: properties and applications, *RSC Adv.*, 2017, **7**, 16801–16822.
22 A. K. Singh, P. Kumar, D. J. Late, A. Kumar, S. Patel and J. Singh, 2D layered transition metal dichalcogenides (MoS2): Synthesis, applications and theoretical aspects, *Appl. Mater. Today*, 2018, **13**, 242–270.
23 F. Hui, C. Pan, Y. Shi, Y. Ji, E. Grustan-Gutierrez and M. Lanza, On the use of two dimensional hexagonal boron nitride as dielectric, *Microelectron. Eng.*, 2016, **163**, 119–133.
24 P. R. Jubu, O. S. Obaseki, D. I. Ajayi, E. Danladi, K. M. Chahrour, A. Muhammad, J. S. Landi, T. Igbawua, H. F. Chahul and F. K. Yam, Considerations about the determination of optical bandgap from diffuse reflectance spectroscopy using the tauc plot, *J. Opt.*, 2024, **53**, 5054–5064.
25 C. Liu and R. Bai, Adsorptive removal of copper ions with highly porous chitosan/cellulose acetate blend hollow fiber membranes, *J. Membr. Sci.*, 2006, **284**, 313–322.
26 V. Mamleev, S. Bourbigot and J. Yvon, Kinetic analysis of the thermal decomposition of cellulose: The main step of mass loss, *J. Anal. Appl. Pyrolysis*, 2007, **80**, 151–165.
27 C. F. Toncón-Leal, J. Villarroel-Rocha, M. T. P. Silva, T. P. Braga and K. Sapag, Characterization of mesoporous region by the scanning of the hysteresis loop in adsorption–desorption isotherms, *Adsorption*, 2021, **27**, 1109–1122.
28 K. S. W. Sing and R. T. Williams, Physisorption Hysteresis Loops and the Characterization of NanoporousMaterials, *Adsorpt. Sci. Technol.*, 2004, **22**, 773–782.
29 L. O. Amaral and A. L. Daniel-da-Silva, MoS2 and MoS2 Nanocomposites for Adsorption and Photodegradation of Water Pollutants: A Review, *Molecules*, 2022, **27**, 6782.
30 G. G. Welegergs, H. G. Gebretinsae, M. T. Girmay, A. Sindelo, A. Tedla, Z. Y. Nuru, S. Nuru, S. Dube, M. Malik and T. Nyokong, Plasmonic Silver (Ag) Supported Mesoporous CuO Nanocomposites for Photodegradation of Methylene Blue in Water, *Catal. Lett.*, 2025, **155**, 275.
31 J. Wu, F. Xu, S. Li, P. Ma, X. Zhang, Q. Liu, R. Fu and D. Wu, Porous polymers as multifunctional platforms, *Adv. Mater.*, 2019, **31**, 1802922.
32 S. Jayabal, G. Saranya, J. Wu, Y. Liu, D. Geng and X. Meng, Understanding the high-electrocatalytic performance of two-dimensional MoS2 nanosheets and their composite materials, *J. Mater. Chem. A*, 2017, **5**, 24540–24563.
33 Z. Zheng, M. Cox and B. Li, Surface modification of hexagonal boron nitride nanomaterials: a review, *J. Mater. Sci.*, 2018, **53**, 66–99.
34 Q. Liu, C. Hu and X. Wang, One-pot solvothermal synthesis of water-soluble boron nitride nanosheets and fluorescent boron nitride quantum dots, *Mater. Lett.*, 2019, **234**, 306–310.
35 M. A. Hussain, M. Yang, T. J. Lee, J. W. Kim and B. G. Choi, High density decoration of noble metal nanoparticles on polydopamine-functionalized molybdenum disulphide, *J. Colloid Interface Sci.*, 2015, **451**, 216–220.
36 X. Shen, J. Wang and G. Xin, Effect of the Zeta Potential on the Corrosion Resistance of Electroless Nickel and PVDF Composite Layers Using Surfactants, *ACS Omega*, 2021, **6**, 33122–33129.
37 P. Bansal, G. R. Chaudhary and S. K. Mehta, Comparative study of catalytic activity of ZrO2 nanoparticles for sonocatalytic and photocatalytic degradation of cationic and anionic dyes, *Chem. Eng. J.*, 2015, **280**, 475–485.
38 M. Bilal, I. Ihsanullah, M. U. H. Shah, A. V. B. Reddy and T. M. Aminabhavi, Recent advances in the removal of dyes from wastewater using low-cost adsorbents, *J. Environ. Manage.*, 2022, **321**, 115981.
39 L. G. Devi and R. Kavitha, A review on non metal ion doped titania for the photocatalytic degradation of organic pollutants under UV/solar light: Role of photogenerated charge carrier dynamics in enhancing the activity, *Appl. Catal., B*, 2013, **140**, 559–587.
40 A. Haleem, A. Shafiq, S. Q. Chen and M. Nazar, A Comprehensive Review on Adsorption, Photocatalytic and Chemical Degradation of Dyes and Nitro-Compounds over Different Kinds of Porous and Composite Materials, *Molecules*, 2023, **28**, 1081.
41 N. M. Mahmoodi, M. Arami, N. Y. Limaee and N. S. Tabrizi, Kinetics of heterogeneous photocatalytic degradation of reactive dyes in an immobilized TiO2 photocatalytic reactor, *J. Colloid Interface Sci.*, 2006, **295**, 159–164.
42 Y. J. Yuan, P. Wang, Z. Li, Y. Wu, W. Bai, Y. Su, G. Jie, S. Wu, J. Zhong, Z. T. Yu and Z. Zou, The role of bandgap and interface in enhancing photocatalytic H2 generation activity of 2D-2D black phosphorus/MoS2 photocatalyst, *Appl. Catal., B*, 2019, **242**, 1–8.
43 E. German and R. Gebauer, Why are MoS2 monolayers not a good catalyst for the oxygen evolution reaction?, *Appl. Surf. Sci.*, 2020, **528**, 146591.
44 M. Laghaei, M. Ghasemian, W. Lei, L. Kong and Q. Chao, A review of boron nitride-based photocatalysts for carbon dioxide reduction, *J. Mater. Chem. A*, 2023, **11**, 11925–11963.

Open Access Article. Published on 19 December 2025. Downloaded on 4/5/2026 8:17:09 PM.
This article is licensed under a Creative Commons Attribution-NonCommercial 3.0 Unported Licence.

45 J. Puls, S. A. Wilson and D. Hölter, Degradation of Cellulose Acetate-Based Materials: A Review, *J. Polym. Environ.*, 2011, **19**, 152–165.
46 S. Selvaraj, K. Natesan, P. B. Bhargav and A. Nafis, Revolutionizing water treatment: Exploring the efficacy of MoS2/BN/rGO ternary nanocomposite in organic dye treated water for OER and HER applications, *J. Water Process Eng.*, 2023, **54**, 104033.
47 F. C. Tompkins, Adsorption isotherms for non-uniform surfaces, *Trans. Faraday Soc.*, 1950, **46**, 580–586.
48 N. Setarehshenas, S. H. Hosseini and G. Ahmadi, Optimization and Kinetic Model Development for Photocatalytic Dye Degradation, *Arabian J. Sci. Eng.*, 2018, **43**, 5785–5797.
49 M. Vigdorowitsch, A. Pchelintsev, L. Tsygankova and E. Tanygina, Freundlich Isotherm: An Adsorption Model Complete Framework, *Appl. Sci.*, 2021, **11**, 8078.

© 2026 The Author(s). Published by the Royal Society of Chemistry